Computational Materials Science 174 (2020) 109501

Contents lists available at ScienceDirect

Computational Materials Science

journal homepage: www.elsevier.com/locate/commatsci

Elastic constants of pure body-centered cubic Mg in nanolaminates

Yanqing Su[a,*], Milan Ardeljan[b], Marko Knezevic[b], Manish Jain[c], Siddhartha Pathak[c], Irene J. Beyerlein[a,d]

[a] Department of Mechanical Engineering, University of California, Santa Barbara, CA 93106-5070, USA
[b] Department of Mechanical Engineering, University of New Hampshire, Durham, NH 03824, USA
[c] Department of Chemical and Materials Engineering, University of Nevada, Reno, NV 89557, USA
[d] Materials Department, University of California, Santa Barbara, CA 93016-5050, USA

ARTICLE INFO

Keywords:
Nanostructure
Elastic modulus
Texture
Density functional theory
Pseudo-morphic phase

ABSTRACT

At ambient temperature, pressure, and sufficiently fine layer thicknesses, pure body-centered cubic (bcc) Mg can exist as a pseudo-morphic phase when coherently bonded with a substantially stiffer bcc metal, such as Nb. Compared to the hexagonal close-packed Mg/bcc Nb nanocomposite that exists in the larger layer thicknesses, the bcc Mg/bcc Nb nanocomposite was recently shown to exhibit significantly higher yield stresses and strains to failure. However, because of the morphological, spatial, and crystallographic constraints imposed by nano-layered architecture, the elastic constants of the individual bcc Mg phase cannot be directly measured experimentally. Lack of this fundamental property stands in the way of theoretical and computational modeling of the mechanical properties of the pseudo-morphic bcc phase of Mg. In this work, we employ density functional theory calculations and a strain-energy-based elasticity method to calculate the lattice and elastic constants of pure bcc Mg. For validation of these constants, we combine a set of micropillar compression experiments and microstructurally explicit finite element simulations for the fully bcc Mg/bcc Nb nanolaminate system. We conclude that (i) for the stress-free bcc Mg, the lattice parameter a_0 is 3.581 Å, and the three independent elastic constants C_{11}, C_{12}, and C_{44} are 39.64 GPa, 34.14 GPa, and 31.38 GPa, respectively, and (ii) for the laminated bcc Mg (i.e., a_0 = 3.347 Å), the three elastic constants are 84.68 GPa, 56.68 GPa, and 61.4 GPa, respectively.

1. Introduction

Bi-phase interface strain engineering has been shown to transform hexagonal close packed (hcp) phases into meta-stable cubic phases at ambient temperatures and pressures [1–6]. The layer thicknesses at which these so-called pseudo-morphic phases persist are very fine, with nanometer dimensions. Recently, this phenomenon was used to transform pure Mg from its low symmetry hcp structure to the more symmetric body-centered cubic (bcc) structure by sandwiching it between another bcc metal, such as Nb, in a nanolaminate architecture [7–9]. This approach, which uses interface strains, is the only way to make pure bcc Mg at ambient temperature and pressure, to the best of our knowledge. Pure Mg in bcc form is only stable under extremely high pressures (50 ± 6 GPa) [13,14]. Here we emphasize the purity of Mg. With some alloying elements at sufficient concentration, the alloyed Mg can be stabilized as a cubic structure, either bcc and face centered cubic (fcc), at ambient temperatures [10–12].

It was recently demonstrated via nanomechanical testing that the pseudo-morphic bcc Mg when coherently bonded to Nb within a nanolaminate exhibited excellent properties [7,9]. Compared to pure hcp Mg, standalone pure bcc Mg withstood much higher strains to failure (60% higher), was 50% stronger, and retained its strength after exposure to 200 °C (0.5 times its homologous temperature) for one hour. The outcome indicates that bcc Mg is a highly attractive pseudo-morphic phase from a structural viewpoint. Bcc Mg may operate by similar easy glide deformation mechanisms, like regular bcc metals, and hence, may be just as ductile and formable [7,9]. Such a prospect is exciting, particularly for the intrinsically lightweight pure Mg metal, which in its stable, ambient hcp form is brittle at room temperature.

To date, many very basic properties of the pseudo-morphic bcc Mg phase that are critical for understanding its structural behavior are not known. First and foremost, its elastic properties have not been measured. Understanding and modeling the deformation mechanisms and the deformation behavior of bcc Mg requires knowing the elastic moduli. For instance, calculations of the critical thickness at which the pseudo-morphic phase of Mg occurs demand knowledge of its elastic moduli. Developing an interatomic potential for pseudo-morphic bcc Mg would call for the elastic moduli for fitting purposes. Much of the

* Corresponding author.
E-mail address: yanqingsu@ucsb.edu (Y. Su).

https://doi.org/10.1016/j.commatsci.2019.109501
Received 16 September 2019; Received in revised form 22 December 2019; Accepted 23 December 2019

outstanding plastic behavior of bcc Mg can be attributed to a change in the structure, motion, and modes of the dislocations of the bcc structure from those of the hcp structure. Calculating the stresses and energies associated with dislocation motion and dislocation-dislocation interactions in bcc Mg via analytical or crystal plasticity modeling would also need the elastic moduli as input.

Several features of the nanostructure of the bcc Mg/bcc Nb preclude use of conventional means to measure its moduli. The elastic properties of thin films have been traditionally measured using either non-contact or contact techniques. Non-contact techniques include acoustic microscopy, laser ultrasonics, micromechanical resonator-based sensing methods [15–26]. Examples of contact techniques are macroscale tensile testing and nanoindentation testing. The non-contact-based techniques have an inherent disadvantage in that it is often complicated to distinguish the response of the thin film from the substrate. The challenges surrounding elastic moduli measurement are also compounded for thin films composed of multiple nanoscale thick layers. The numerous heterophase interfaces in the films can result in multiple internal reflections. The epitaxial nature of growth within the individual layers, along with the high surface area-to-volume ratio of 2D layering, result in significant anisotropy in the elastic response. The layers are not single crystalline but nanocrystalline, comprised of many grains distributed in crystallographic orientation. Both classes of measurement techniques are unable to discern the anisotropy of the elastic properties, because the fine nanoscale volume of the Mg layer confined between Nb layers prevents direct mechanical testing of the Mg alone.

One very recent attempt was made to use synchrotron X-ray diffraction (XRD) to measure the bulk modulus of the pseudo-morphic bcc Mg phase [27]. The study analyzed Mg/Nb nanolaminates with a 1:1 layer thickness ratio and ranging from 5 nm to 50 nm in layer thickness. The measurements indicated that, for an hcp-to-bcc pseudo-morphic phase transformation in Mg, the critical layer thickness lies between 7 and 8 nm. In particular, the crystal structure of the 5 nm/5 nm laminate was found to be uniformly bcc and the lattice parameter for the Mg and Nb phases was equivalent: $a_0 = 3.347$ Å. Both Mg and Nb phases were highly textured with the {1 1 0} pole oriented along the nanolaminate thickness. The combined data indicate that the {1 1 0}Mg||{1 1 0}Nb interface is coherent and the orientation relationship cube-on-cube.

The synchrotron XRD data showed that the peaks of the pseudo-morphic bcc Mg and the bcc Nb structures overlap and hence they were not able to differentiate between the two structures [27]. The bulk modulus values calculated from the bcc Mg/bcc Nb 5 nm/5 nm nanolaminates and the bcc Nb peaks in the hcp Mg/bcc Nb 50 nm/50 nm nanolaminates are all similar and match the value corresponding to bulk Nb. Thus, in bcc Mg/bcc Nb 5 nm/5 nm nanolaminates, the bulk modulus computed from the peaks correspond to that of bcc Nb but not bcc Mg. To date, the elastic constants of bcc Mg are unknown experimentally.

Density functional theory (DFT) is a common method for calculating the moduli of a perfect crystal. In Ref. [28], a DFT model supercell of bcc Mg was created and the elastic constants calculated via a stress-strain method. The elastic constants C_{11}, C_{12}, and C_{44} were calculated to be 35.55 GPa, 35.23 GPa, and 29 GPa, respectively. The results imply that bcc Mg is much softer than Nb, as well as hcp Mg. However, with the predicted constants, the first of three Born stability criteria for cubic crystals, $C_{11} > C_{12}$, is barely satisfied [29]. Latter DFT work estimated these constants to be 38 GPa, 33 GPa, and 23.8 GPa, respectively [30].

In this work, we combine DFT, full-field 3D microstructural modeling with explicit grain structures, and micropillar compression to predict and validate the elastic constants of the pseudo-morphic bcc Mg phase. Unlike previous studies, here, the DFT calculation for the elastic constants includes a large number of valence electrons and the strain-energy method. To validate the DFT predictions, we utilize focused ion beam (FIB)-fabricated micro-pillar compression experiments to characterize the anisotropic elastic response of the nanolayered composite. To obtain three distinct curves, micropillars are fabricated with interfaces oriented either normal, parallel and oblique (45°) to the compression axis. Each configuration generates unique mechanical information. Compression normal and parallel to the interface represent approximate iso-stress and iso-strain orientations, while the compression test obliquely to the layers can provide information on the elastic shear response. Use of the DFT lattice and elastic constants in the micromechanical model produced composite elastic responses in full agreement with all measurements. We conclude that (i) for the stress-free bcc Mg, the elastic constants C_{11}, C_{12}, and C_{44} are 39.64 GPa, 34.14 GPa, and 31.38 GPa, respectively, and (ii) for the laminated bcc Mg, the three elastic constants are 84.68 GPa, 56.68 GPa, and 61.4 GPa, respectively. Based on these values, we reveal that bcc Mg is elastically soft compared to other structural bcc metals and highly elastically anisotropic.

2. Methodologies

2.1. Two possible cases

As mentioned, prior measurements with high pressure XRD synchrotron were performed for the 5 nm/5 nm bcc Mg/bcc Nb nanolaminate (hereinafter referred to as the *bcc Mg nanolaminate*). It was found that the composite bulk modulus was 180 GPa. Two distinct possibilities can explain this result. The first, termed case A, is that only the stiffness of Nb is being measured. The measured bulk modulus of 180 GPa is very close to that of bulk Nb (~178.33 GPa). This case recognizes the possibility of a giant stiffness mismatch, wherein the stiffness of the bcc Mg could be significantly lower than that of Nb. Nb preserves its stiffness constants, C_{11}^{Nb}, C_{12}^{Nb}, and C_{44}^{Nb}, whereas the stiffness of the pseudo-morphic phase of bcc Mg is unknown. Presuming that the stiffness of bcc Mg exhibits cubic anisotropy, we are left with three unknowns, C_{11}^{A}, C_{12}^{A}, and C_{44}^{A}.

The second possibility, termed case B, is that bcc Mg and bcc Nb have the same elastic stiffness. This case considers that the stiffness of nanolayered Nb and Mg are both modified by the formation of the coherent Mg/Nb interface. The three unknowns are the three cubic stiffness constants C_{11}^{B}, C_{12}^{B}, and C_{44}^{B} common to the adjoined coherent Mg/Nb pair.

Two independent approaches are used to estimate the elastic moduli of bcc Mg. The first employs DFT, in which 10 valence electrons are used in the calculation, and state-of-the-art algorithms for elastic moduli estimation from DFT simulations. The second approach combines micropillar compression on the nanolaminates and a micromechanics model [31], in which the elastic deformation of the layered, textured nanostructure is simulated. For case A, we directly incorporate the DFT calculated constants for bcc Mg into the simulation of the bcc Mg/Nb nanocomposite compression response and compare it with the experimental deformation tests. For case B, we determine the elastic constants for which the micromechanical model reproduces all three curves based on micropillar compression. Such micromechanical approach has been used on martensite in steels [32].

2.2. Density functional theory

DFT calculations were conducted using VASP [33]. Based on the projector augmented wave method [34,35], three pseudopotentials are employed, with different numbers of valence electrons for which a plane-wave basis with a cutoff energy of 600 eV is adopted. To approximate the exchange-correlation energy functional, the Perdew-Burke-Ernzerhof formulation of the generalized gradient approximation is used [36]. The conjugate gradient scheme is employed for the electronic self-consistent loop; the convergence is reached when the total free energy change between two steps are smaller than 10^{-4} eV. The Brillouin zone is constructed by the Monkhorst-Pack scheme [37], with a smearing width of 0.2 eV based on the Methfessel-Paxton smearing method [38].

A periodic cell containing two atoms is used to determine the lattice parameter a_0 and elastic constants C_{11}, C_{12}, and C_{44}. The k-point mesh is 19 × 19 × 19. For a_0, the simulation cell size is varied, with the free energy calculated for each size, and a_0 corresponds to the one with the lowest free energy. The elastic constants are calculated via the energy-strain method provided in AELAS [39].

2.3. Micromechanics model

In this paper, we focus on the bcc Mg nanolaminate, which has coherent interfaces. As a feasibility check, however, the investigation is also applied to the much thicker 50 nm/50 nm Mg/Nb nanocomposite (referred to as the *hcp Mg nanolaminate*).

2.3.1. Micropillar compression

In order to compare pseudo-morphic bcc Mg with hcp Mg, multilayers were synthesized using physical vapor deposition, as in prior works [7,9,32]. The depositions aimed to create two sets of layer thicknesses: 5 nm/5 nm and 50 nm/50 nm Mg/Nb nanocomposites. Then transmission electron microscopy (TEM) was used to measure the actual layer thicknesses. The bcc Mg nanolaminate was found to have almost equal Mg and Nb layer thicknesses of about 5.5 nm, and the hcp Mg nanolaminate and a Mg layer thickness of ~35 nm and a Nb layer thickness ~65 nm. In the former composite, XRD and TEM verified that the Mg phase uniformly has a bcc crystal structure, Mg and Nb have the same texture, and the interface is coherent. In the latter composite, the Mg phase is hcp, the interfaces are incoherent, and the elastic constants of both phases are well known by measurements independent from the ones we employ here.

To determine the composite stiffness, we conducted micropillar compression tests on the bcc Mg nanolaminates and on the hcp Mg nanolaminates. The micropillars were fabricated in the dual beam FEI Helios™ FIB Scanning Electron Microscopy (SEM), using a beam of Ga+ ions to remove the material and shape it in pillar form. Details of the micropillar fabrication and in-site testing are described in prior work [7]. The same micropillar tests were used in both cases A and B, each of which introduces three unknowns. Micropillars with layers oriented at three distinct angles with respect to the pillar axis (which is the compression axis) are made. Specialized FIB-fabricated techniques are used to make micropillar compression with interfaces that were oblique (45°) to the compression axis. If the Mg and Nb crystals are elastically anisotropic, each composite layer orientation would be expected to produce a different composite modulus under compression.

2.3.2. FE modeling

To model the composite elastic response, we employ the finite element (FE) method. An important component of FE modeling is building the 3D microstructure model, including the layer morphology, intralayer grain shapes, and texture of each phase [40,41]. A second component is the deformation simulation, including boundary conditions, and the third one concerns the constitutive law, which we consider to be linear elastic for each phase. The first two components are described in turn below. The third one pertains to the objective of the paper, which is to characterize the elastic constants, and is discussed in more detail with the presentation of the results.

The initial 5 nm/5 nm Mg/Nb microstructures for the FE calculations are based on the experimental measurements. The models for the normal and parallel micropillar tests are the same. Fig. 1 shows the meshed model of the Mg/Nb bilayer. The models are divided into two equal volumes that represent a layer of the Nb bonded to a layer of Mg. Both layers are polycrystalline in plane and single crystalline through thickness with one grain spanning the layer thickness. The grains are made 100 nm wide and thus, have a pancake-like shape. The grain microstructure is periodic. The FE meshes consist of roughly 435,000 C3D4 elements in Abaqus (i.e., continuum three-dimensional four-nodal elements). Each layer consists of 267 grains or a total of 534 grains in both layers.

A special custom procedure is developed to generate FE granular models where the composite layers are built 45° angle with respect to the loading axis. This procedure is different from the one utilized to generate FE models for calculating the normal and parallel material responses. A schematic of the model is shown in Fig. 1, where a layer thickness of 50 nm is used as an example. The main idea is to first create a 3D voxel-based model of the granular microstructure that contains a large number of layers and then to perform a cut that would ultimately give us a desired microstructural model [42]. Each individual layer (which contains grains of appropriate size and shape) was separately generated in DREAM.3D [43] and then assembled in a big/large scale voxel-based model using a Matlab script. Next, using the same script, we define a cutting profile to mask/select voxels from the interior of the layered model. We choose a cutting profile that allows us to obtain a voxel-based model with layers that are 45° inclined with respect to the global axes (Fig. 2). An important fact to emphasize here is that the cutting is performed on the voxel-based model and not on the FE model. To achieve a better representation of the grain structure within the 45° voxel-based model, we perform Laplacian based smoothing filter implemented in DREAM.3D to smooth out and suppress any serrated boundaries between grains. After applying the filter, the surface meshes of all individual grains in the model are obtained. Next, we proceed with performing their solid meshing (mesh interior of each grain) in MSC Patran [44]. Finally, we generate an FE model of the granular microstructure (Fig. 2) that is composed of linear tetrahedral C3D4 elements. Material (elastic) properties of Mg and Nb are alternately prescribed for all the layers in the microstructure.

We simulate compression deformation in all microstructural models. In the loading direction, the displacement is prescribed; in the lateral direction, the surfaces were kept free to expand. Note that the loading, applied normal and parallel to the Mg/Nb interfaces, respectively, is along the negative z and negative x direction. Periodic boundary conditions are used. To impose them, the deformation of the pairs, left/right, top/bottom, and front/back faces, are made equal and the stress tensors on each pair set to be opposite in sign.

At every integration point in these model microstructures, the constitutive law accounts for cubic elastic anisotropy [45,46], which for a cubic material leaves three unknown elastic constants. In case A, the three unknowns correspond to the elastic constants for the bcc Mg phase, or in case B, to the combined bcc Mg/Nb phase. The same three 5 nm/5 nm microstructural models are used for cases A and B. As a test of the model, we also build a normal, parallel, and 45° model of the hcp Mg/Nb nanolaminate, in which the elastic constants of the hcp Mg and bcc Nb are already known [9].

It is worth noting that recent experiments in [27] found that in the 5 nm/5 nm laminate, the bcc Mg and bcc Nb phases share the same lattice parameter of 3.347 Å. The change in lattice parameter generates coherency stresses and strains. An analytical calculation of these stresses using the DFT elastic constants can be found in Appendix A. The normal in-plane stresses in the bcc Mg and bcc Nb are –1.4 GPa and 1.45 GPa, respectively. The coherency stress is, however, localized and only influences local behavior, such as crack nucleation and eventual ductility/fracture. However, in a large volume, such as the micropillars being modeled here, the coherency stresses become broadly distributed and in equilibrium across the sample volume, which would not appreciably affect the homogenized properties of the sample, such as elasticity, and the macroscopic elastic stress-strain response [47]. Accordingly, the local coherency stresses were not taken into account in the micromechanical simulation.

3. Results

In this section, we present results from DFT calculations and the micromechanics model. Known elastic constants of hcp Mg and bcc Nb are given in Table 1.

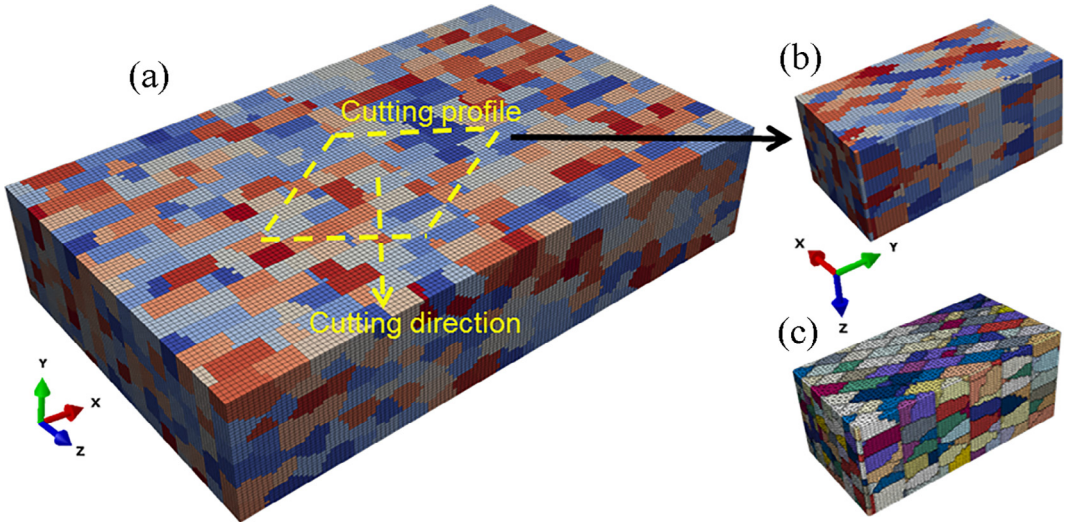

Fig. 1. Schematic of the developed procedure for 45° finite element model generation. (a) Large scale voxel-based model that contains large number of layers used for cutting, (b) 45° voxel-based model obtained as a result of cutting, (c) corresponding 45° FE model.

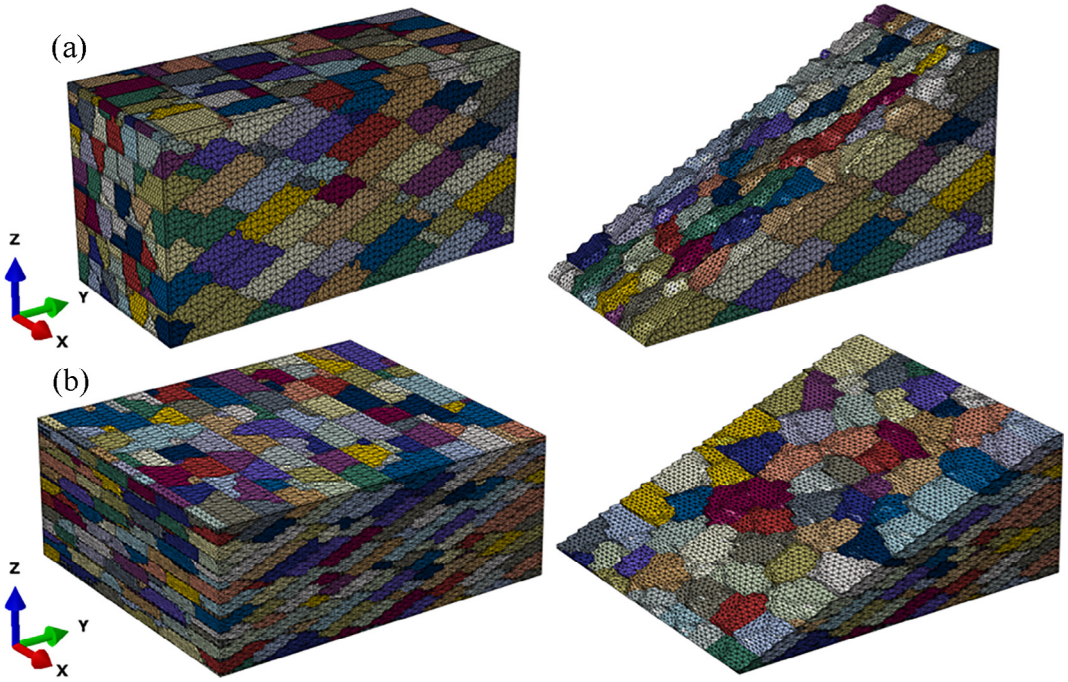

Fig. 2. FE models of an explicit grain structure with 45° layer configuration where the layer thickness is (a) 50 nm and (b) 5 nm. Right hand images reveal the interior of the granular microstructure.

3.1. DFT predictions

DFT calculations were carried out assuming different number of valence electrons in the pseudo-potential. The results are summarized in Table 2. Among our calculations, we observe a sensitivity in C_{11} only to the number of valence electrons used. Both C_{11} and a_0 are the largest based on the 10 valence-electron pseudo-potential (i.e., Mg_sv) compared to those for 2 and 8 valence-electron calculations. To further validate the Mg_sv potential, we use it to calculate the lattice parameters and elastic constants of hcp Mg. A comparison with experimental results presented in Table 3 shows that the Mg_sv potential provides accurate predictions for the lattice parameters and reasonable predictions for the elastic constants. Therefore, in the remainder of this paper, DFT predictions based on Mg_sv will be considered.

Table 1
Experimental values of single crystal elastic constants for hcp Mg and bcc Nb, respectively, at room temperature and under zero external stress [48,49].

hcp Mg					bcc Nb		
C_{11}(GPa)	C_{12}(GPa)	C_{13}(GPa)	C_{33}(GPa)	C_{44}(GPa)	C_{11}(GPa)	C_{12}(GPa)	C_{44}(GPa)
59.4	25.61	21.44	61.6	16.4	246	134	28.7

Table 2
DFT calculations of the lattice parameter a_0, cohesive energy E_{coh}, elastic constants C_{11}, C_{12}, and C_{44} for bcc Mg at 0 K under zero external stress. PAW: project augmented wave.

PAW potential	number of valence electrons	a_0 (Å)	E_{coh} (eV)	C_{11} (GPa)	C_{12} (GPa)	C_{44} (GPa)
Mg	2	3.575	–1.478	37.62	34.83	31.41
Mg_pv	8	3.577	–1.477	37	34.68	31.17
Mg_sv	10	3.581	–1.500	39.64	34.14	31.38
Mg [28]	2	3.574	–1.487	35	35	29
Mg [30]	unknown	3.571	–1.453	38.07	33.07	23.77

The same quantities were previously calculated by DFT in Refs. [28,30]. The lattice parameters and elastic constants from all three calculations conducted here differ from those previously reported using two [28] or an unknown number of valence electrons [30]. Apart from the number of valence electrons used in the calculation, the differences can be explained by choice of cut-off energy, *k*-point numbers, and the method to calculate the moduli. Unlike in the present work which uses a strain-energy method following a recent DFT work [50], these two studies used the stress-strain method to calculate the elastic constants. Further, compared with the current work, the study by Junkaew et al. [30] used a coarser *k*-point grid of 18 × 18 × 18 and a lower cutoff energy of 520 eV. In general, a denser *k*-point grid and a higher cutoff energy can reduce potential errors in DFT calculations.

All calculations indicate that the elastic anisotropy of bcc Mg is relatively high. We use the Zener ratio, $A_c = 2C_{44}/(C_{11} - C_{12})$, and its deviation from unity, as a measure of the elastic anisotropy. For the calculations here, compared to the 2- and 8-valence electron calculation, the 10-valence electron case gives the lowest Zener ratio A_c of 11.4, and that from Ref. [30] is 9.5. These values are higher than that of Lithium (9.14), which possesses the highest Zener ratio among all bcc elemental metals [51].

The corresponding bulk modulus ($K_b = (C_{11} + 2C_{12})/3$) for bcc Mg is 35.97 GPa, which is higher than but still close to that of bulk hcp Mg (32.5 GPa) measured experimentally (see Table 1). Yet, the bcc bulk modulus is substantially lower than the experimentally measured bulk modulus of Nb (178.33 GPa). The significantly lower bulk modulus of the bcc phase supports case A, in which the measured 180 GPa bulk modulus of the composite corresponds to that of Nb.

We recall in the 5 nm/5 nm laminate, the bcc Mg and bcc Nb phases share the same lattice parameter of 3.347 Å. Using this lattice parameter, we calculate the elastic constants of bcc Mg and bcc Nb. As shown in Table 4, the elastic constants in both phases increase from those associated with the lattice parameter of their unlaminated, free state, particularly for bcc Mg. This calculation implies that due to the alteration of the lattice parameter alone, a dramatic change in the elastic constants for bcc Mg can be expected.

3.2. Estimates from the micromechanics model

First, to demonstrate the feasibility of the approach, we apply the model to the hcp Mg nanolaminates. In prior XRD studies, the bulk modulus values of hcp Mg in this nanolaminate coincide with those measured for the bulk (non-laminated) hcp Mg. Accordingly, the microstructure model uses input for the elastic properties of the hcp Mg phase and bcc Nb phase as summarized in Table 1. Fig. 3 compares the microstructural model elastic stress-strain responses for all three tests with the experiments. Also shown are the SEM images of the pillars after failure (beyond the elastic regime). The agreement between the simulated response and measurement is excellent, verifying the modeling approach we developed here. Table 5 provides the composite moduli estimates from the tests, where the error bars reflect the dispersion from the two tests.

Table 4
DFT calculations of the lattice parameter a_0, elastic constants C_{11}, C_{12}, and C_{44} for bcc Mg and bcc Nb at 0 K. PAW: project augmented wave. Row 2: under zero external stress. Row 3 and row 4: when the two materials have the same experimentally measured laminated lattice parameter of 3.347 Å.

PAW potential	a_0 (Å)	C_{11} (GPa)	C_{12} (GPa)	C_{44} (GPa)
Nb	3.324	233.39	126.78	14.35
Nb	3.347	249.01	135.43	18.1
Mg_sv	3.347	84.68	56.68	61.4

Next, we consider the bcc Mg nanolaminates. To prove repeatability, two experimental tests are conducted for each layer-load orientation. Fig. 4 shows the elastic responses as well as SEM images of the pillars after the test to failure. Each layer orientation gives a distinct composite modulus, indicating that one or the other or both of the phases is elastically anisotropic. Table 5 summarizes the composite moduli measured for each test. The error bars in modulus are calculated based on the differences among the two tests. On the FE side, the same modeling approach used in the hcp Mg nanocomposites is employed. The two separate cases introduced earlier are considered.

We first test case A, in which the goal is to find the values of C_{11}, C_{12}, and C_{44} of bcc Mg that enable the composite model to fit all three curves very well, while at the same time, satisfying the Born mechanical stability criterion, $C_{11} > C_{12}$. Fig. 4 shows that the model for case A achieves good agreement. The corresponding moduli for bcc Mg are $C_{11}^A = 65$ GPa, $C_{12}^A = 35$ GPa, and $C_{44}^A = 22.5$ GPa (See Table 6). Accordingly, the bulk modulus of bcc Mg is 45 GPa. This value is substantially lower than that of Nb (178 GPa), but not too far from the DFT prediction (35.97 GPa). It could, therefore, be argued that it was too low to be measured *in-situ* in the recent XRD tests on this same multilayer nanolaminate material [27]. We use the Zener ratio, $A_c = 2C_{44}^A/(C_{11}^A - C_{12}^A)$, and its deviation from unity, as a measure of the elastic anisotropy. The moduli for bcc Mg from case A indicates that $A_c = 1.5$, which relative to many cubic materials is not considered significantly anisotropic. In fact, like hcp Mg, bcc Mg in case A is nearly elastically isotropic.

The same procedure is used in case B to find the values of C_{11}^B, C_{12}^B, and C_{44}^B that enable the composite model to fit all three curves well, while at the same time, satisfying the Born mechanical stability criterion, $C_{11}^B > C_{12}^B$. In Fig. 5, the modeling predictions for case B are compared with the same experimental curves in Fig. 4. The corresponding elastic constants shared by bcc Mg and bcc Nb are $C_{11}^B = 100$ GPa, $C_{12}^B = 20$ GPa, and $C_{44}^B = 25$ GPa (Table 6). From case B, the value of A_c is 0.625. It is not unlike a bcc material to have a Zener ratio less than one. For instance, $A_c = 0.43$ for bulk Nb and 0.7219 for

Table 3
Experimental measurements [48] and DFT calculations of the lattice parameter *a* and *c*, elastic constants C_{11}, C_{12}, C_{13}, C_{33}, and C_{44} for hcp Mg at 0 K under zero external stress.

Method	*a* (Å)	*c* (Å)	C_{11} (GPa)	C_{12} (GPa)	C_{13} (GPa)	C_{33} (GPa)	C_{44} (GPa)
Experiment [48]	3.187	5.17	63.48	25.94	21.7	66.45	18.42
DFT (Mg_sv)	3.184	5.167	58.55	32.85	23.55	62.88	19.98
DFT [28]	3.192	5.178	63	27	20	69	18
DFT [30]	3.198	5.184	72.7	18.99	17.88	69.54	17.83

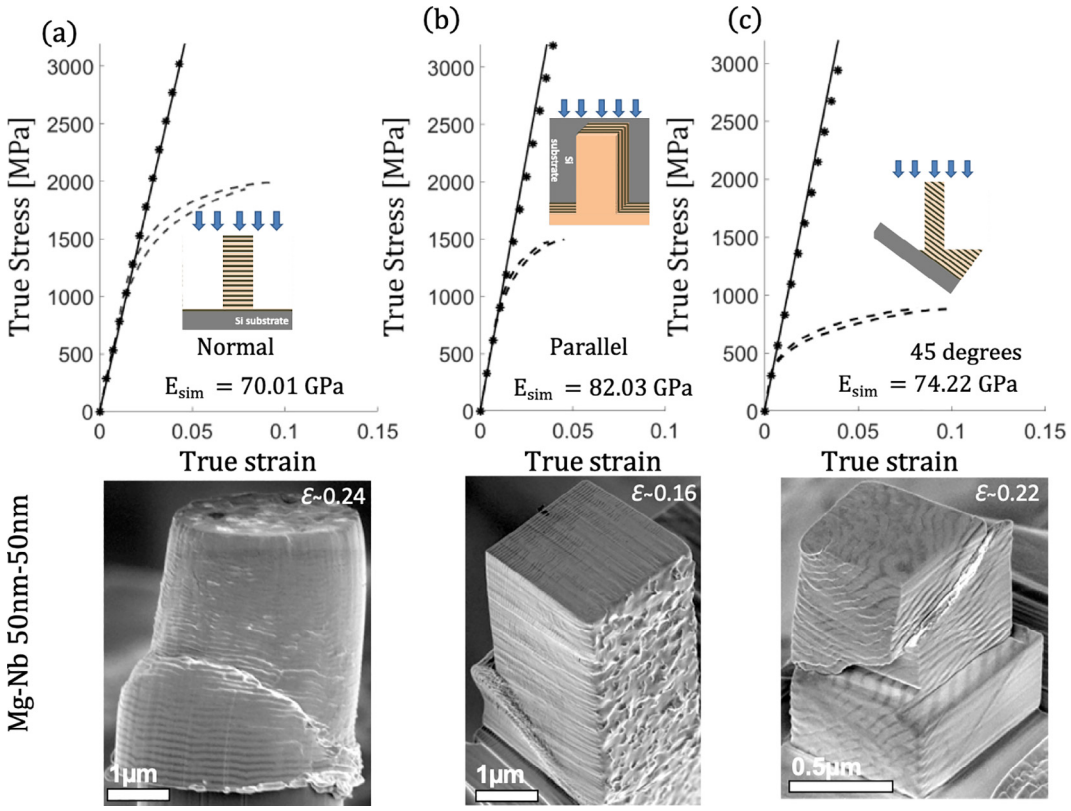

Fig. 3. Comparison of the measured and calculated elastic stress-strain curves for the hcp Mg nanocomposite: (a) normal, (b) parallel and (c) 45° cases. This case is used for validating the model since all the elastic constants are known (see Table 1). In the remainder of this paper, all stress-strain curves use dashed lines for the experimental values from Ref. [9], black lines for the extrapolated elastic response averaged from the two experimental samples in each case, and asterisks * for the FE results obtained in the current work. Corresponding SEM images of the pillars after the test to failure (beyond the elastic regime).

Table 5
Experimentally measured composite Young's moduli from the micropillar tests.

nanolaminate	Layer normal (GPa)	Layer parallel (GPa)	Layer 45° (GPa)
hcp Mg/bcc Nb nanolaminate	69.5 ± 3.3	88.7 ± 13	81.2 ± 8.5
bcc Mg/bcc Nb nanolaminate	76.5 ± 4.8	93.27 ± 11.3	82.9 ± 7

bulk Mo [51]. However, the bulk modulus corresponding to the case B elastic constants is 46.67 GPa for both bcc Mg and bcc Nb, which is much lower than that measured by XRD (180 GPa). The large discrepancy implies that case B is not valid. It is, therefore, not likely that the bcc Mg and bcc Nb nanolayers adopt the same elastic moduli in the composite.

3.3. DFT-informed FE simulations

Here, we perform a set of FE deformation simulations for compression of the three-layer orientations using the elastic constants for bcc Mg from DFT (Table 2) and for bcc Nb from bulk measurements (Table 1). Fig. 6 compares the simulation results with the experimental micropillar tests. The agreement is reasonably good. Deviations are likely caused by the idealized layer morphology in the model, which are not perfectly planar in the micropillars. Nevertheless, we emphasize that the FE calculation does not involve any unknown elastic constants or adjustments to the elastic constants.

4. Discussion

The main goal of this work is to determine the elastic constants of the pseudo-morphic bcc phase of nanocrystalline Mg at room temperature and ambient pressure. We used two independent methods to calculate the moduli, one involving DFT and another involving micromechanics calculations. Unlike prior efforts, the former method, DFT, used 10 valence electrons and a strain-energy method for elastic constant calculations. For the stress-free bcc Mg, DFT predicts the lattice parameter a_0 is 3.581 Å, and 39.64 GPa, 34.14 GPa, and 31.38 GPa for C_{11}, C_{12}, and C_{44}, respectively. For the laminated bcc Mg (i.e., a_0 = 3.347 Å), the three elastic constants are 84.68 GPa, 56.68 GPa, and 61.4 GPa, respectively. These values differ from prior DFT reports and satisfy the Born stability criterion.

Validation of the DFT predictions is needed but must be carried out indirectly since direct measurements of the elastic constants of bcc Mg are not available and to date, are challenging to obtain. The validation step involves the second micromechanics method, which is newly presented here. It provides a basic technique to determine the elastic moduli of a confined, textured nanocrystalline phase(s) when the composite elastic stress-strain response is known. The nanolayer composite elasticity measurements include nanolaminates tested in compression normal, parallel, and at an oblique angle to the nanolayers. For simulating the latter test, non-periodic microstructure that cannot be replicated using standard microstructural building techniques. As part of this study, it was necessary to develop a computational method for representing inclined layers, an algorithm presented in detail in Section 2.3.2.

Recent XRD measurements of bulk modulus for the bcc Mg

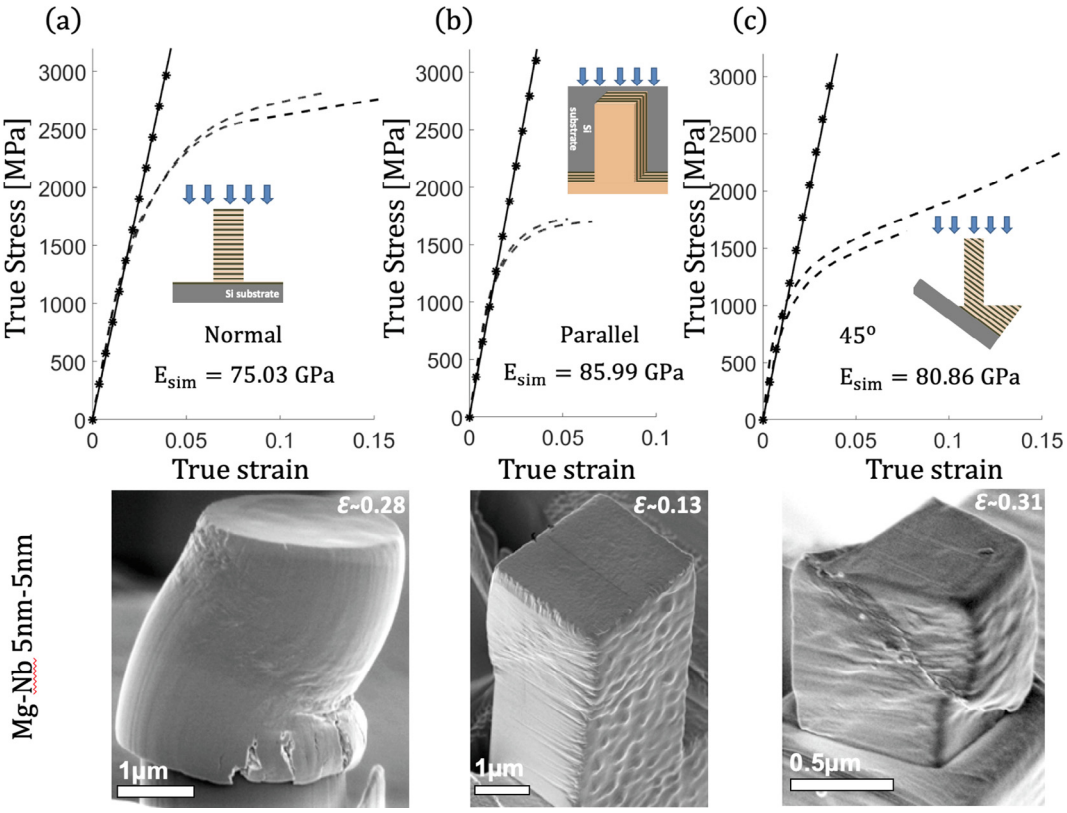

Fig. 4. (top row) Comparison of case A elastic stress-strain curves with experiment for the bcc Mg nanocomposite (a) normal, (b) parallel and (c) 45° cases. (bottom row) Corresponding SEM images of the pillars after the test to failure (beyond the elastic regime).

Table 6
Values of single crystal elastic constants determined from the micromechanics model for the two cases at room temperature. In case A, the elastic constants for bcc Mg were unknown while those for bcc Nb were taken from Table 1. In case B, the elastic constants, which were assumed to be the same for bcc Mg and bcc Nb, were unknown.

	bcc Mg			bcc Nb		
	C_{11}(GPa)	C_{12}(GPa)	C_{44}(GPa)	C_{11}(GPa)	C_{12}(GPa)	C_{44}(GPa)
Case A	65	35	22.5	246	134	28.7
Case B	100	20	25	100	20	25

nanocomposites reported that the composite modulus was 180 GPa, close to that of unlaminated, bulk Nb (178.33 GPa). Based on this finding, two possible explanations for the sets of elastic constants in the Mg bcc phase were hypothesized. In case A, the bulk modulus of bcc Mg was assumed to be different from that of bcc Nb. In case B, bcc Mg and bcc Nb were assumed to have the same bulk modulus. The DFT calculations find that the bulk modulus of bcc Mg (35.97 GPa) is far lower than that of Nb (178.33 GPa), indicating that case A is more likely. The micromechanical model produced a single set of three constants under the assumption of case B to reproduce simultaneously all three distinct elastic responses from the micropillar tests. The bulk modulus corresponding to this fitting process was 45 GPa, which is far below that measured by high-pressure synchrotron measurements (180 GPa). Again, case A evidently is the more likely scenario compared to case B.

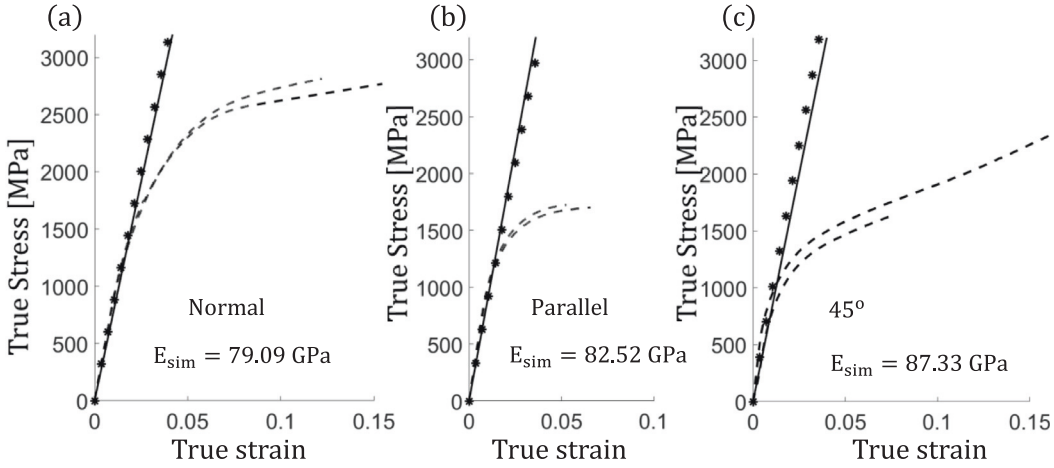

Fig. 5. Comparison of case B elastic stress-strain curves with experiment for the bcc Mg nanocomposite (a) normal, (b) parallel and (c) 45° cases.

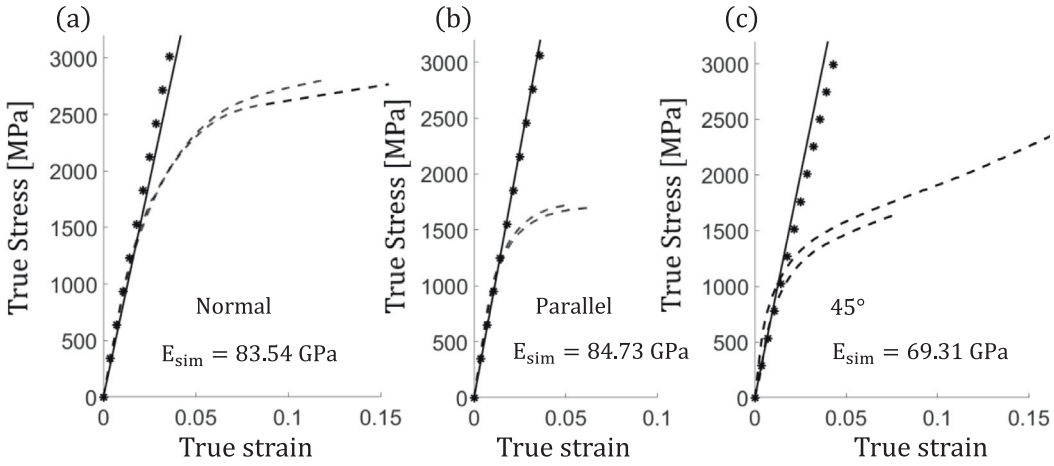

Fig. 6. Comparison of the DFT-informed FE calculations of elastic stress-strain curves with experiment for the bcc Mg nanocomposite (a) normal, (b) parallel and (c) 45° interface cases.

For validation of the DFT elastic moduli, we sought to determine whether the DFT-calculated moduli for bcc Mg lie in the range of constants that would lead to agreement between the micromechanical model and the experimental response in composite pillar tests. Indeed, when the DFT-calculated elastic moduli of bcc Mg are used in FE simulations, good agreement with the experimental values is achieved. Yet, there was some deviations between the simulated and measured elastic responses, and as with any modeling procedure, validation and discrepancies need to be addressed. First, the micromechanical method is validated against hcp Mg/Nb nanolaminate data. Second, the DFT calculations are carried out at 0 K and not at room temperature. Third, the approach involves measuring and simulating composite moduli for only three distinct orientations. Including the composite elastic responses in other types of deformation tests, such as shear tests, or for other oblique angles, would have further constrained the model, narrowing even more the range of possible values for each elastic constant. Yet, still, despite these differences, the agreement seen in Fig. 6 is excellent. Thus, from this study, we conclude that the elastic moduli for the pseudo-morphic bcc phase of pure Mg correspond to those calculated by DFT.

One intriguing aspect of the DFT predictions is the large elastic anisotropy of bcc Mg, corresponding to a Zener ratio of 11.4. Structural bcc metals have Zener ratios that are usually much lower, such as Fe, which has a ratio of 2.46 [51]. In crystals, the large elastic anisotropy tends to yield strong interactions between screw and edge components [52], activate unusual slip systems [53], affect the dislocation core structure [54], line tension [55], dislocation loop shape [56], and Frank-Read source activation [57].

Last, we note that all FE models and experiments in this paper are under ambient pressure. Nevertheless, the aforementioned XRD-based bulk modulus of bcc Mg nanocomposite, 180 GPa, was based on data taken over a broad span of pressures ranging from ambient to 60 GPa [27], far above the hcp-to-bcc transition pressure of 45 GPa for Mg. To check the effects of the pressure on the elastic constants, we applied the same DFT method to bcc Mg and bcc Nb at 45 GPa. At this pressure, the lattice parameters were found to be 3.043 and 3.125 Å, respectively, for bcc Mg and bcc Nb. The elastic constants for bcc Mg are C_{11} = 180.86 GPa, C_{12} = 108.4 GPa, C_{44} = 130.85 GPa and for bcc Nb, they are C_{11} = 422.3 GPa, C_{12} = 196.8 GPa, C_{44} = 53.21 GPa. Thus, under 45 GPa, the bulk moduli for bcc Mg and bcc Nb are 132.55 GPa and 272 GPa respectively, leading to a volume average bulk modulus of 202.77 GPa. This value is still not far from the measured 180 GPa bulk modulus of the bcc Mg nanocomposites.

5. Conclusions

In this paper, we utilize two independent approaches, DFT and a newly proposed micromechanics model, to obtain the elastic constants of bcc Mg, which exists when an Mg nanolayer is sandwiched between bcc Nb layers in nanocomposites. Both methods exclude the possibility that the bcc Mg and bcc Nb nanolayers, when laminated in a composite, adopt the same elastic moduli, and show that bcc Mg is softer than hcp Mg, and is much softer than bcc Nb. Our analyses estimate that for the stress-free bcc Mg phase, the lattice constant a_0 is 3.581 Å and the three independent elastic constants, C_{11}, C_{12}, and C_{44}, are 39.64 GPa, 34.14 GPa, and 31.38 GPa, respectively. For the laminated bcc Mg (i.e., a_0 = 3.347 Å), the three elastic constants are 84.68 GPa, 56.68 GPa, and 61.4 GPa, respectively. As an added contribution, the micromechanics nanolayered composite model we present here is readily applicable to estimate the elastic moduli of one phase if those of the other phase and the overall nanocomposite are known.

CRediT authorship contribution statement

Yanqing Su: Formal analysis, Methodology, Investigation, Software, Writing - original draft, Writing - review & editing. **Milan Ardeljan:** Formal analysis, Methodology, Investigation, Software, Writing - review & editing. **Marko Knezevic:** Resources, Software. **Manish Jain:** Formal analysis, Investigation, Resources. **Siddhartha Pathak:** Supervision, Funding acquisition, Writing - review & editing. **Irene J. Beyerlein:** Conceptualization, Supervision, Funding acquisition, Writing - original draft, Writing - review & editing.

Declaration of Competing Interest

The authors declare that they have no known competing financial interests or personal relationships that could have appeared to influence the work reported in this paper.

Acknowledgements

Y.S. and I.J.B. acknowledge financial support from the National Science Foundation NSF CMMI-1728224 (UCSB). M.A. and M.K. acknowledge financial support from the National Science Foundation (NSF CMMI-1727495). SP and MJ acknowledge funding from NSF MRI #1726897 and NSF CMMI #1841331 for this work. The authors would like to thank Dr. Xiangguo Li for help discussions. Use was made of computational facilities purchased with funds from the National Science Foundation (CNS-1725797) and administered by the Center for

Scientific Computing (CSC). The CSC is supported by the California NanoSystems Institute and the Materials Research Science and Engineering Center (MRSEC; NSF DMR 1720256) at UC Santa Barbara. This work used the Extreme Science and Engineering Discovery Environment (XSEDE), which is supported by National Science Foundation grant number ACI-1053575.

Appendix A

Here, we estimate the coherency strain/stress in the 5 nm/5 nm Mg/Nb bilayer composite. Let the z direction be normal to the bimetal interface. The transformation strains in hcp Mg and bcc Nb, respectively, are

$$\Delta_{11}^{\mathrm{Mg}} = \Delta_{22}^{\mathrm{Mg}} = \frac{a_0 - a_0^{\mathrm{Mg}}}{a_0^{\mathrm{Mg}}} = \frac{3.347 - 3.209}{3.209} = 0.043 \tag{A.1}$$

$$\Delta_{11}^{\mathrm{Nb}} = \Delta_{22}^{\mathrm{Nb}} = \frac{a_0 - a_0^{\mathrm{Nb}}}{a_0^{\mathrm{Nb}}} = \frac{3.347 - 3.301}{3.301} = 0.014 \tag{A.2}$$

where a_0^{Mg} and a_0^{Nb}, taken from Ref. [51], are the basal plane lattice parameter of hcp Mg and the lattice parameter of bcc Nb in their respective free states, and a_0, experimentally measured in Ref. [27], is the common lattice parameter of the 5 nm/5 nm bcc Mg/bcc Nb system. According to Shoykhet et al. [58], the elastic stress tensors in bcc Mg and bcc Ng, respectively, are

$$\sigma_{\mathrm{ela}}^{\mathrm{Mg}} = \begin{bmatrix} M^{\mathrm{Mg}}A^{\mathrm{Mg}} & 0 & 0 \\ 0 & M^{\mathrm{Mg}}A^{\mathrm{Mg}} & 0 \\ 0 & 0 & 0 \end{bmatrix} \tag{A.3}$$

$$\sigma_{\mathrm{ela}}^{\mathrm{Nb}} = \begin{bmatrix} M^{\mathrm{Nb}}A^{\mathrm{Nb}} & 0 & 0 \\ 0 & M^{\mathrm{Nb}}A^{\mathrm{Nb}} & 0 \\ 0 & 0 & 0 \end{bmatrix} \tag{A.4}$$

where ν is the isotropic Poisson's ratio, $M = 2\mu(1+\nu)/(1-\nu)$ is the isotropic biaxial modulus, where μ is the isotropic shear modulus, and

$$A^{\mathrm{Mg}} = \frac{M^{\mathrm{Mg}}\Delta_{11}^{\mathrm{Mg}} + M^{\mathrm{Nb}}\Delta_{11}^{\mathrm{Nb}}}{M^{\mathrm{Mg}} + M^{\mathrm{Nb}}} - \Delta_{11}^{\mathrm{Mg}} \tag{A.5}$$

$$A^{\mathrm{Nb}} = \frac{M^{\mathrm{Mg}}\Delta_{11}^{\mathrm{Mg}} + M^{\mathrm{Nb}}\Delta_{11}^{\mathrm{Nb}}}{M^{\mathrm{Mg}} + M^{\mathrm{Nb}}} - \Delta_{11}^{\mathrm{Nb}} \tag{A.6}$$

Using the Voigt average for cubic systems [59], μ and ν, respectively, are

$$\mu = \frac{1}{5}(3C_{44} + C_{11} - C_{12}) \tag{A.7}$$

$$\nu = \frac{C_{11} + 4C_{12} - 2C_{44}}{4C_{11} + 6C_{12} + 2C_{44}} \tag{A.8}$$

To obtain the upper bound of the elastic strain tensor, we use the elastic constants of bcc Mg and bcc Nb corresponding to a common lattice parameter $a_0 = 3.347$Å at 0 K, which are presented in Table 4. As such,

$$\mu^{\mathrm{Mg}} = \frac{1}{5}(3 \times 61.4 + 84.68 - 56.68) = 42.44 \ \ \mathrm{GPa} \tag{A.9}$$

$$\mu^{\mathrm{Nb}} = \frac{1}{5}(3 \times 18.1 + 249.01 - 135.43) = 33.58 \ \ \mathrm{GPa} \tag{A.10}$$

$$\nu^{\mathrm{Mg}} = \frac{84.68 + 4 \times 56.68 - 2 \times 61.4}{4 \times 84.68 + 6 \times 56.68 + 2 \times 61.4} = 0.235 \tag{A.11}$$

$$\nu^{\mathrm{Nb}} = \frac{249.01 + 4 \times 135.43 - 2 \times 18.1}{4 \times 249.01 + 6 \times 135.43 + 2 \times 18.1} = 0.409 \tag{A.12}$$

Hence

$$M^{\mathrm{Mg}} = \frac{2 \times 42.44 \times (1 + 0.235)}{1 - 0.235} = 137.03 \ \ \mathrm{GPa} \tag{A.13}$$

$$M^{\mathrm{Nb}} = \frac{2 \times 33.58 \times (1 + 0.409)}{1 - 0.409} = 160.12 \ \ \mathrm{GPa} \tag{A.14}$$

$$A^{\mathrm{Mg}} = \frac{137.03 \times 0.043 + 160.12 \times 0.014}{137.03 + 160.12} - 0.043 = -0.016 \tag{A.15}$$

$$A^{\mathrm{Nb}} = \frac{137.03 \times 0.043 + 160.12 \times 0.014}{137.03 + 160.12} - 0.014 = 0.013 \tag{A.16}$$

Therefore, the upper bounds of the elastic strains are

$$\sigma_{\mathrm{ela}}^{\mathrm{Mg}} = \begin{bmatrix} -2.19 & 0 & 0 \\ 0 & -2.19 & 0 \\ 0 & 0 & 0 \end{bmatrix} \mathrm{GPa} \tag{A.17}$$

$$\sigma_{ela}^{Nb} = \begin{bmatrix} 2.08 & 0 & 0 \\ 0 & 2.08 & 0 \\ 0 & 0 & 0 \end{bmatrix} \text{GPa} \tag{A.18}$$

To obtain the lower bound of the elastic strain tensor, we use the elastic constants of hcp Mg and bcc Nb under zero external stress at room temperature, which are presented in Table 1. As such,

$$\mu^{Mg} = \frac{1}{5}(3 \times 16.4 + 59.4 - 25.61) = 16.6 \ \text{GPa} \tag{A.19}$$

$$\mu^{Nb} = \frac{1}{5}(3 \times 28.7 + 246 - 134) = 39.62 \ \text{GPa} \tag{A.20}$$

$$\nu^{Mg} = \frac{59.4 + 4 \times 25.61 - 2 \times 16.4}{4 \times 59.4 + 6 \times 25.61 + 2 \times 16.4} = 0.304 \tag{A.21}$$

$$\nu^{Nb} = \frac{246 + 4 \times 134 - 2 \times 28.7}{4 \times 246 + 6 \times 134 + 2 \times 28.7} = 0.393 \tag{A.22}$$

Hence

$$M^{Mg} = \frac{2 \times 16.6 \times (1 + 0.304)}{1 - 0.304} = 62.2 \ \text{GPa} \tag{A.23}$$

$$M^{Nb} = \frac{2 \times 39.62 \times (1 + 0.393)}{1 - 0.393} = 181.85 \ \text{GPa} \tag{A.24}$$

$$A^{Mg} = \frac{62.2 \times 0.043 + 181.85 \times 0.014}{62.2 + 181.85} - 0.043 = -0.022 \tag{A.25}$$

$$A^{Nb} = \frac{62.2 \times 0.043 + 181.85 \times 0.014}{62.2 + 181.85} - 0.014 = 0.007 \tag{A.26}$$

Therefore, the lower bounds of the elastic strains are

$$\sigma_{ela}^{Mg} = \begin{bmatrix} -1.37 & 0 & 0 \\ 0 & -1.37 & 0 \\ 0 & 0 & 0 \end{bmatrix} \text{GPa} \tag{A.27}$$

$$\sigma_{ela}^{Nb} = \begin{bmatrix} 1.27 & 0 & 0 \\ 0 & 1.27 & 0 \\ 0 & 0 & 0 \end{bmatrix} \text{GPa} \tag{A.28}$$

As an intermediate estimate of the elastic strain tensor, we use the elastic constants of bcc Mg obtained in case A and those of bcc Nb measured experimentally [49], both at room temperature, under zero external stress, and presented in Table 6. As such,

$$\mu^{Mg} = \frac{1}{5}(3 \times 22.5 + 65 - 35) = 19.5 \ \text{GPa} \tag{A.29}$$

$$\mu^{Nb} = \frac{1}{5}(3 \times 28.7 + 246 - 134) = 39.62 \ \text{GPa} \tag{A.30}$$

$$\nu^{Mg} = \frac{65 + 4 \times 35 - 2 \times 32.5}{4 \times 65 + 6 \times 35 + 2 \times 32.5} = 0.262 \tag{A.31}$$

$$\nu^{Nb} = \frac{246 + 4 \times 134 - 2 \times 28.7}{4 \times 246 + 6 \times 134 + 2 \times 28.7} = 0.393 \tag{A.32}$$

Hence

$$M^{Mg} = \frac{2 \times 19.5 \times (1 + 0.262)}{1 - 0.262} = 66.69 \ \text{GPa} \tag{A.33}$$

$$M^{Nb} = \frac{2 \times 39.62 \times (1 + 0.393)}{1 - 0.393} = 181.85 \ \text{GPa} \tag{A.34}$$

$$A^{Mg} = \frac{66.69 \times 0.043 + 181.85 \times 0.014}{66.69 + 181.85} - 0.043 = -0.021 \tag{A.35}$$

$$A^{Nb} = \frac{66.69 \times 0.043 + 181.85 \times 0.014}{66.69 + 181.85} - 0.014 = 0.008 \tag{A.36}$$

Therefore, the intermediate estimates of the elastic strains are

$$\sigma_{ela}^{Mg} = \begin{bmatrix} -1.4 & 0 & 0 \\ 0 & -1.4 & 0 \\ 0 & 0 & 0 \end{bmatrix} \text{GPa} \tag{A.37}$$

$$\sigma_{ela}^{Nb} = \begin{bmatrix} 1.45 & 0 & 0 \\ 0 & 1.45 & 0 \\ 0 & 0 & 0 \end{bmatrix} \text{GPa} \tag{A.38}$$

References

[1] W.P. Lowe, T.H. Geballe, NbZr multilayers. I. Structure and superconductivity, Phys Rev B 29 (1984) 4961–4968, https://doi.org/10.1103/PhysRevB.29.4961.

[2] G.B. Thompson, R. Banerjee, S.A. Dregia, H.L. Fraser, Phase stability of bcc Zr in Nb/Zr thin film multilayers, Acta Mater 51 (2003) 5285–5294, https://doi.org/10.1016/S1359-6454(03)00380-X.

[3] J.Y. Zhang, P. Zhang, X. Zhang, R.H. Wang, G. Liu, G.J. Zhang, J. Sun, Mechanical properties of fcc/fcc Cu/Nb nanostructured multilayers, Mater Sci Eng, A 545 (2012) 118–122, https://doi.org/10.1016/j.msea.2012.03.009.

[4] R. Ahuja, H.L. Fraser, Microstructural transitions in Titanium-Aluminum thin film multilayers, J Electron Mater 23 (1994) 1027–1034, https://doi.org/10.1007/BF02650371.

[5] R. Banerjee, R. Ahuja, H.L. Fraser, Dimensionally induced structural transformations in titanium-aluminum multilayers, Phys Rev Lett 76 (1996) 3778–3781, https://doi.org/10.1103/PhysRevLett. 76.3778.

[6] J.Q. Zheng, J.B. Ketterson, G.P. Felcher, Synthesis of layered crystals of titanium silver, J Appl Phys 53 (1982) 3624–3628, https://doi.org/10.1063/1.331143.

[7] S. Pathak, N. Velisavljevic, J.K. Baldwin, M. Jain, S. Zheng, N.A. Mara, I.J. Beyerlein, Strong, ductile, and thermally stable bcc-Mg nanolaminates, Sci Rep 7 (2017) 8264, https://doi.org/10.1038/s41598-017-08302-5.

[8] B. Ham, X. Zhang, High strength Mg/Nb nanolayer composites, Mater Sci Eng, A 528 (2011) 2028–2033, https://doi.org/10.1016/j.msea.2010.10.101.

[9] M. Ardeljan, M. Knezevic, M. Jain, S. Pathak, A. Kumar, N. Li, N.A. Mara Nathan, J.K. Baldwin, I.J. Beyerlein, Room temperature deformation mechanisms of Mg/Nb nanolayered composites, J Mater Res 33 (2018) 1311–1332, https://doi.org/10.1557/jmr.2018.107.

[10] Y. Ogawa, D. Ando, Y. Sutou, J. Koike, A lightweight shape-memory magnesium alloy, Science 353 (2016) 368–370, https://doi.org/10.1126/science.aaf6524.

[11] W. Xu, N. Birbilis, G. Sha, Y. Wang, J.E. Daniels, Y. Xiao, M. Ferry, A high-specific-strength and corrosion-resistant magnesium alloy, Nat Mater 14 (2015) 1229–1235, https://doi.org/10.1038/nmat4435.

[12] O. Pavlic Olivia, W. Ibarra-Hernandez, I. Valencia-Jaime, S. Singh, G. Avendaño-Franco, D. Raabe, A.H. Romero, Design of Mg alloys: the effects of Li concentration on the structure and elastic properties in the Mg-Li binary system by first principles calculations, J Alloys Comps 691 (2017) 15–25, https://doi.org/10.1016/j.jallcom.2016.08.217.

[13] H. Olijnyk, W.B. Holzapfel, High-pressure structural phase transition in Mg, Phys Rev B 31 (1985) 4682–4683, https://doi.org/10.1103/PhysRevB.31.4682.

[14] G.W. Stinton, S.G. MacLeod, H. Cynn, D. Errandonea, W.J. Evans, J.E. Proctor, Y. Meng, M.I. McMahon, Equation of state and high-pressure/high-temperature phase diagram of magnesium, Phys Rev B 90 (2014) 134105, , https://doi.org/10.1103/PhysRevB.90.134105.

[15] D. Bhattacharyya, N.A. Mara, P. Dickerson, R.G. Hoagland, A. Misra, Compressive flow behavior of Al-TiN multilayers at nanometer scale layer thickness, Acta Mater 59 (2011) 3804–3816, https://doi.org/10.1016/j.actamat.2011.02.036.

[16] N.A. Mara, I.J. Beyerlein, Review: effect of bimetal interface structure on the mechanical behavior of Cu–Nb fcc–bcc nanolayered composites, J Mater Sci 49 (2014) 6497–6516, https://doi.org/10.1007/s10853-014-8342-9.

[17] M.J. Bamber, K.E. Cooke, A.B. Mann, B. Derby, Accurate determination of Young's modulus and Poisson's ratio of thin films by a combination of acoustic microscopy and nanoindentation, Thin Solid Films 398–399 (2001) 299–305, https://doi.org/10.1016/S0040-6090(01)01341-4.

[18] F. Zhang, S. Krishnaswamy, D. Fei, D.A. Rebinsky, B. Feng, Ultrasonic characterization of mechanical properties of Cr- and W-doped diamond-like carbon hard coatings, Thin Solid Films 503 (2006) 250–258, https://doi.org/10.1016/j.tsf.2005.11.057.

[19] Y.Y. Kim, An advanced characterization method for the elastic modulus of nanoscale thin-films using a high-frequency micromechanical resonator, Materials 10 (2017) 806, https://doi.org/10.3390/ma10070806.

[20] Donald O. Thompson, Dale E. Chimenti (Eds.), Review of progress in quantitative nondestructive evaluation, Springer US, Boston, MA, 1998.

[21] N.A. Mara, D. Bhattacharyya, R.G. Hoagland, A. Misra, Tensile behavior of 40nm Cu/Nb nanoscale multilayers, Scr Mater 58 (2008) 874–877, https://doi.org/10.1016/j.scriptamat.2008.01.005.

[22] Y. Kihara, T. Nagoshi, T.M. Chang, H. Hosoda, S. Tatsuo, M. Sone, Tensile behavior of micro-sized specimen made of single crystalline nickel, Mater Lett 153 (2015) 36–39, https://doi.org/10.1016/j.matlet.2015.03.119.

[23] T. Chudoba, N. Schwarzer, F. Richter, Determination of elastic properties of thin films by indentation measurements with a spherical indenter, Surf Coat Technol 127 (2000) 9–17, https://doi.org/10.1016/S0257-8972(00)00552-1.

[24] S. Pathak, N. Li, X. Maeder, R.G. Hoagland, J.K. Baldwin, J. Michler, A. Misra, J. Wang, N.A. Mara, On the origins of hardness of Cu-TiN nanolayered composites, Scr Mater 109 (2015) 48–51, https://doi.org/10.1016/j.scriptamat.2015.07.015.

[25] D. Bhattacharyya, N.A. Mara, R.G. Hoagland, A. Misra, Nanoindentation and microstructural studies of Al/TiN multilayers with unequal volume fractions, Scr Mater 58 (2008) 981–984, https://doi.org/10.1016/j.scriptamat.2008.01.054.

[26] J. Domke, M. Radmacher, Measuring the elastic properties of thin polymer films with the atomic force microscope, Langmuir 14 (1998) 3320–3325, https://doi.org/10.1021/la9713006.

[27] M. Jain, N. Velisavljevic, J.K. Baldwin, M. Knezevic, N.A. Mara, I.J. Beyerlein, S. Pathak, Structure and properties of pseudomorphically transformed bcc Mg in Mg/Nb multilayered nanolaminates studied using synchrotron X-ray diffraction, J Appl Phys 126 (2019) 025302, , https://doi.org/10.1063/1.5097249.

[28] A. Kumar, I.J. Beyerlein, J. Wang, First-principles study of the structure of Mg/Nb multilayers, Appl Phys Lett 105 (2014) 071602, , https://doi.org/10.1063/1.4893700.

[29] M. Born, On the stability of crystal lattices. I, Mathem Proc Cambridge Philos Soc 36 (1940) 160–172, https://doi.org/10.1017/S0305004100017138.

[30] A. Junkaew, B. Ham, X. Zhang, A. Talapatra, R. Arróyave, Stabilization of bcc Mg in thin films at ambient pressure: experimental evidence and *ab initio* calculations, Mater Res Lett 1 (2013) 161–167, https://doi.org/10.1080/21663831.2013.804218.

[31] M. Ardeljan, I.J. Beyerlein, M. Knezevic, A dislocation density based crystal plasticity finite element model: application to a two-phase polycrystalline HCP/BCC composites, J Mech Phys Solids 66 (2014) 16–31, https://doi.org/10.1016/j.jmps.2014.01.006.

[32] A.M. Cantara, M. Zecevic, A. Eghtesad, C.M. Poulin, M. Knezevic, Predicting elastic anisotropy of dual-phase steels based on crystal mechanics and microstructure, Int J Mech Sci 151 (2019) 639–649, https://doi.org/10.1016/j.ijmecsci.2018.12.021.

[33] G. Kresse, J. Furthmüller, Efficient iterative schemes for ab initio total-energy calculations using a plane-wave basis set, Phys Rev B 54 (1996) 11169, https://doi.org/10.1103/PhysRevB.54.11169.

[34] P.E. Blöchl, Projector augmented-wave method, Phys Rev B 50 (1994) 17953, https://doi.org/10.1103/PhysRevB.50.17953.

[35] G. Kresse, D. Joubert, From ultrasoft pseudopotentials to the projector augmented-wave method, Phys Rev B 59 (1999) 1758, https://doi.org/10.1103/PhysRevB.59.1758.

[36] J.P. Perdew, K. Burke, M. Ernzerhof, Generalized gradient approximation made simple, Phys Rev Lett 77 (1996) 3865, https://doi.org/10.1103/PhysRevLett. 77.3865.

[37] J. Monkhorst, J.D. Pack, Special points for Brillouin-zone integrations, Phys Rev B 13 (1976) 5188, https://doi.org/10.1103/PhysRevB.13.5188.

[38] M. Methfessel, A.T. Paxton, High-precision sampling for Brillouin-zone integration in metals, Phys Rev B 40 (1989) 3616, https://doi.org/10.1103/PhysRevB.40.3616.

[39] S.H. Zhang, R.F. Zhang, AELAS: Automatic ELAStic property derivations via high-throughput first-principles computation, Comp Phys Commun 220 (2017) 403–416, https://doi.org/10.1016/j.cpc.2017.07.020.

[40] M. Ardeljan, D.J. Savage, A. Kumar, I.J. Beyerlein, M. Knezevic, The plasticity of highly oriented nano-layered Zr/Nb composites, Acta Mater 115 (2016) 189–203, https://doi.org/10.1016/j.actamat.2016.05.058.

[41] M. Ardeljan, M. Knezevic, T. Nizolek, I.J. Beyerlein, N.A. Mara, T.M. Pollock, A study of microstructure-driven strain localizations in two-phase polycrystalline HCP/BCC composites using a multi-scale model, Int J Plast 74 (2015) 35–57, https://doi.org/10.1016/j.ijplas.2015.06.003.

[42] T.J. Barrett, D.J. Savage, M. Ardeljan, M. Knezevic, An automated procedure for geometry creation and finite element mesh generation: Application to explicit grain structure models and machining distortion, Comput Mater Sci 141 (2018) 269–281, https://doi.org/10.1016/j.commatsci.2017.09.048.

[43] DREAM.3D Version 4.2, BlueQuartz Software, Springboro, OH, USA; 2013. http://dream3d.bluequartz.net/.

[44] Patran Version 2013, MSC Software Corporation, Newport Beach, CA, USA; 2013. https://www.mscsoftware.com/product/patran.

[45] M. Knezevic, B. Drach, M. Ardeljan, I.J. Beyerlein, Three dimensional predictions of grain scale plasticity and grain boundaries using crystal plasticity finite element models, Comput Methods Appl Mech Eng 277 (2014) 239–259, https://doi.org/10.1016/j.cma.2014.05.003.

[46] Beyerlein IJ, Knezevic M. Springer International Publishing AG, part of Springer Nature 2018 W. Andreoni S. Yip (Eds.), Handbook of Materials Modeling, https://doi.org/10.1007/978-3-319-42913-7_82-1.

[47] P.J. Withers, H.K.D.H. Bhadeshia, Residual stress. Part I – Measurement techniques, Mater Sci Technol 17 (2001) 355, https://doi.org/10.1179/026708301101509980.

[48] L.J. Slutsky, C.W. Garland, Elastic constants of magnesium from 4.2° K to 300° K, Physical Review 107 (1957) 972, https://doi.org/10.1103/PhysRev. 107.972.

[49] D.I. Bolef, Elastic constants of single crystals of the bcc transition elements V, Nb, and Ta, J Appl Phys 32 (1961) 100, https://doi.org/10.1063/1.1735933.

[50] Y. Su, S. Xu, I.J. Beyerlein, Density functional theory calculations of generalized stacking fault energy surfaces for eight face-centered cubic transition metals, J Appl Phys 126 (2019) 105112, , https://doi.org/10.1063/1.5115282.

[51] H. Warlimont, W. Martienssen (Eds.), Springer handbook of materials data, 2nd ed., Springer Handbooks (Springer International Publishing), 2018https://doi.org/10.1007/978-3-319-69743-7.

[52] D. Hull, D.J. Bacon, Introduction to dislocations, 5th ed., Butterworth-Heinemann, 2011.

[53] H.L. Heinisch, G. Jr, J.W. Sines, S.H. Kirby Goodman, Elastic stresses and self-energies of dislocations of arbitrary orientation in anisotropic media: olivine, orthopyroxene, calcite, and quartz, J Geophys Res 80 (1975) 1885–1896, https://doi.org/10.1029/JB080i014p01885.

[54] S. Xu, Y. Su, I.J. Beyerlein, Modeling dislocations with arbitrary character angle in face-centered cubic transition metals using the phase-field dislocation dynamics method with full anisotropic elasticity, Mech Mater 139 (2019) 103200, , https://doi.org/10.1016/j.mechmat.2019.103200.

[55] D.N. Blaschke, B.A. Szajewski, Line tension of a dislocation moving through an anisotropic crystal, Phil Mag 98 (2018) 2397–2424, https://doi.org/10.1080/14786435.2018.1489152.

[56] S.P. Fitzgerald, Z. Yao, Shape of prismatic dislocation loops in anisotropic α-Fe, Philos Mag Lett 89 (2009) 581–588, https://doi.org/10.1080/09500830903199012.
[57] S.P. Fitzgerald, S. Aubry, S.L. Dudarev, W. Cai, Dislocation dynamics simulation of Frank-Read sources in anisotropic α-Fe, Modell Simul Mater Sci Eng 20 (2012) 045022, , https://doi.org/10.1088/0965-0393/20/4/045022.
[58] B. Shoykhet, M.A. Grinfeld, P.M. Hazzledine, Internal stresses and strains in coherent multilayers, Acta Mater 46 (1998) 3761–3766, https://doi.org/10.1016/S1359-6454(97)00244-9.
[59] Y. Su, S. Xu, I.J. Beyerlein, *Ab initio*-informed phase-field modeling of static dislocation core structures in equal-molar CoNiRu multi-principal element alloys, Modell Simul Mater Sci Eng 27 (2019) 084001, , https://doi.org/10.1088/1361-651X/ab3b62.